THE JOURNAL OF PHYSICAL CHEMISTRY C
A JOURNAL OF THE AMERICAN CHEMICAL SOCIETY

pubs.acs.org/JPCC Article

Raman Spectroscopy and Aging of the Low-Loss Ferrimagnet Vanadium Tetracyanoethylene

Hil Fung Harry Cheung, Michael Chilcote, Huma Yusuf, Donley S. Cormode, Yueguang Shi, Seth Kurfman, Andrew Franson, Michael E. Flatté, Ezekiel Johnston-Halperin, and Gregory D. Fuchs*

Cite This: *J. Phys. Chem. C* 2021, 125, 20380−20388 Read Online

ACCESS | Metrics & More | Article Recommendations | Supporting Information

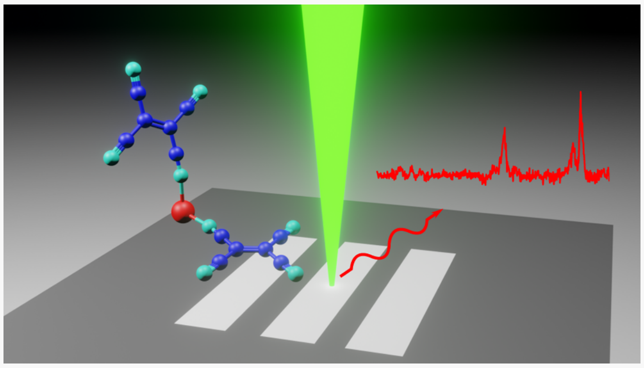

ABSTRACT: We report on micro-focused Raman spectroscopy of encapsulated vanadium tetracyanoethylene (V[TCNE]$_x$, $x \approx 2$) films as they age under ambient conditions to understand the structural changes that accompany aging and how those changes influence the magnetic properties. V[TCNE]$_x$ is an organic-based ferrimagnet with a high magnetic ordering temperature $T_C > 600$ K, low magnetic damping, and growth compatibility with a wide variety of substrates. However, similar to other organic-based materials, it is sensitive to air. Although encapsulation of V[TCNE]$_x$ with glass and epoxy extends the film lifetime from hours to weeks, its aging processes remain poorly understood. We identify the relevant features in the Raman spectra in agreement with *ab initio* theory, reproducing C═C and C≡N stretching vibrational modes. We correlate changes in the Raman intensity and in photoluminescence to changes in the magnetic properties of the sample as measured using ferromagnetic resonance and magnetometry. Based on changes in the Raman spectra, we hypothesize structural changes and aging mechanisms in V[TCNE]$_x$. We also find that we can introduce similar changes using focused laser illumination at high intensity, enabling a new mechanism for "erasing" magnetism in this material through selective modification of local bonding. These findings enable a local optical probe of V[TCNE]$_x$ film quality, which is invaluable in experiments where assessing film quality with local magnetic characterization is not possible, and they enable patterning of V[TCNE]$_x$ by laser writing.

■ INTRODUCTION

In the field of coherent magnonics,[1] where function is derived through the creation and manipulation of long-lived spin-wave modes, an essential property of the host magnetic material is low intrinsic damping. Vanadium tetracyanoethylene (V-[TCNE]$_x$, $x \approx 2$) is an organic-based magnetic material[2−5] with low intrinsic damping[6] comparable to that of yttrium iron garnet (YIG) at room temperature. Its spin waves can be detected with broadband ferromagnetic resonance (FMR), Brillouin light scattering (BLS), and inverse spin Hall effect (ISHE).[7,8] While YIG has been used in many magnonics experiments,[9−15] it has proven to be challenging to integrate high-quality YIG with other materials due to the need for a lattice-matched substrate, e.g., gadolinium gallium garnet (GGG) and an annealing temperature above 800 °C.[16−18] In comparison, V[TCNE]$_x$ can be grown as a thin film using chemical vapor deposition at a modest temperature (50 °C) and on a variety of substrates.[6,19] Furthermore, V[TCNE]$_x$ can be patterned using electron-beam lithography and lift-off techniques without losing its low magnetic damping.[20] It also retains low damping under cryogenic conditions.[21] Hence, it is an attractive alternative for applications in magnonics.

The properties of V[TCNE]$_x$ also make it interesting for coherent quantum magnonics, an emerging field. Coupling between magnons and microwave photons[22−24] or optical photons[25−28] are being actively explored. Recently, the idea of extending coherent magnonics to the quantum level[1] has gained traction[9,29−32] because it promises new mechanisms for coupling together solid-state spins[31,33−36] and superconducting resonators.[10−15,37] For coupling to solid-state spins, the magnetic material has to be patterned for microscale modal confinement while retaining low damping, and the damping must remain low at cryogenic temperatures.[31] This is challenging to achieve in YIG because patterning thin films by aggressive etching increases damping.[38−40] Loss can be improved using lift-off techniques;[41,42] however, the damping is still compromised compared with pristine thin films. Furthermore, at cryogenic temperature, damping in YIG thin

Received: May 25, 2021
Published: September 13, 2021

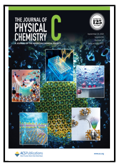

films increases due to coupling to two-level fluctuators.[43−45] Therefore, the properties of V[TCNE]$_x$ make it stand out as a candidate material for quantum magnonic devices.

With these motivations in mind, a materials integration challenge when working with V[TCNE]$_x$ is its air sensitivity, which is similar to many organic-based and molecular materials. The development of encapsulation techniques, similar to those used to protect organic light-emitting diodes (OLEDs) in commercial products,[46−49] can extend its lifetime at room temperature and in ambient atmosphere from hours to weeks.[50] However, the limitations to the lifetime of V[TCNE]$_x$ and its associated aging mechanisms are poorly understood. For example, one aging mechanism is the chemical reaction of V[TCNE]$_x$ with oxygen and water, which turns a V[TCNE]$_x$ film from blue-black opaque to transparent.[50] This is not the only mechanism, however, because aging has been observed in the samples that are stored in an inert environment. Over long times, there are changes to the magnetic properties of the samples that remain opaque. Another piece of evidence is the slowing down of aging when the sample is stored at low temperature (−30 °C) in argon, suggesting an internal change being a significant aging mechanism.

In this work, we study the correlation between the structural and magnetic properties of encapsulated V[TCNE]$_x$ films grown by chemical vapor deposition[6,50] using confocal microscopy, micro-focused Raman spectroscopy, ferromagnetic resonance (FMR), superconducting quantum interference device (SQUID) magnetometry, and *ab initio* calculations to uncover the changes that occur as V[TCNE]$_x$ ages. We discover that as the sample ages under ambient conditions, there are changes in the V−N, C=C, and C ≡ N bonding of V[TCNE]$_x$. These changes are consistent with the reduction of the magnetic moment that we observe, suggesting that as the bonds denature, local magnetism is lost. Our observations are made using micro-focused Raman spectroscopy, showing that a local, optical measurement can be used to assess V[TCNE]$_x$ film quality. Surprisingly, we find that the remaining magnetic material retains its low magnetic damping, which is promising for applications. We also find that the effects of aging are similar to the structural changes induced by local laser heating. Based on this finding, we demonstrate the submicron laser patterning of V[TCNE]$_x$, which points to a useful and convenient method for fabricating magnetic microstructures of this material.

■ METHODS

Sample Growth and Handling. We examine six V[TCNE]$_x$ samples in this work. Sample 1 is a 400 nm V[TCNE]$_x$ film capped with 73 nm of evaporated aluminum and encapsulated with epoxy and a glass coverslip. The thickness is estimated from the growth time. The aluminum layer is designed to block the laser light from exciting fluorescence in the epoxy, ensuring we optically probe only V[TCNE]$_x$. This sample is used for both Raman spectroscopy and aging studies.

Samples 2−6 are encapsulated with glass and epoxy only. Sample 2 is a 1.6 μm thick film used for optical power-dependent measurements. Samples 3 and 4 are 400 nm thick films grown in the same batch. Sample 3 is used for an aging study. Sample 4 is used for low temperature (250 K) photoluminescence (PL) measurements and laser patterning. Sample 5 is a uniform 1 μm thick film grown in 2016. Sample 6 is a patterned 1 μm thick film, with 100 μm wide bars grown in 2018/2019. These two samples are used for long-term aging measurements. When not being measured, the samples are stored at room temperature, either in ambient atmosphere or in a desiccator at reduced pressure (0.2 atmospheric pressure).

***Ab Initio* Calculations.** The electronic structure and phonon modes of V[TCNE]$_x$ are calculated using the Vienna *ab initio* Simulation Package (VASP) (version 5.4.4) with a plane wave basis and projector augmented wave pseudopotentials.[51−54] These pseudopotentials use the generalized gradient approximation (GGA) of Perdew, Burke, and Ernzerhof (PBE).[55] A Hubbard U = 4.19 for the vanadium ion, determined via a linear response method,[56] was used in the phonon calculations. The hybrid functional Heyd−Scuseria−Ernzerhof (HSE)[57] with the standard range separation parameter ω=0.2 was also tested for this system and showed consistent results with the PBE + U approach.

The phonon modes are computed by finite differences: displacing each ion in the V[TCNE]$_x$ unit cell along each of the Cartesian coordinates and then recalculating the energy of the system to evaluate the second energy derivative with respect to displacement. The eigenvalues and eigenmodes of the resulting Hessian matrix represent the mode frequencies and vibration amplitudes. Higher wavenumber (>1400 cm^{-1}) modes are predominantly of C=C or C≡N character and are labeled as C=C or C≡N stretching modes, though the normal mode amplitudes have contributions from every ion.

Optical and Magnetic Measurements. Optical measurements, including micro-focused Raman spectroscopy and photoluminescence, are performed in a homebuilt confocal microscope with a 532 nm continuous wave laser. Photoluminescence collected from the sample is detected using a single-photon counting module, whereas Raman spectra are recorded using a Princeton Instruments spectrometer with a low dark count camera.

We measure angle-resolved, field-modulated FMR in a homebuilt spectrometer. The setup consists of a microwave signal generator, an electromagnet, a pair of modulation coils, a microwave diode detector, and a lock-in amplifier. The film magnetization is measured using a Quantum Design MPMS 3 SQUID magnetometer with an in-plane applied magnetic field. Unless otherwise stated, all measurements presented are performed at room temperature.

■ RESULTS AND DISCUSSION

Raman Spectroscopy. We characterize V[TCNE]$_x$ chemical bonds and structure using Raman spectroscopy. To better understand the collected spectra, we compare them with density functional theory (DFT) calculations performed as described in the Methods section. We show the calculated V[TCNE]$_x$ structure in Figure 1a with a geometry that agrees with previous DFT studies.[58−60] We note V[TCNE]$_x$ is amorphous and the DFT-calculated structure only represents a local structural order.[61] We find that the large wavenumber (>1400 cm^{-1}) DFT normal modes are predominantly C=C or C≡N stretch modes. We show the calculated vibrational modes in Figure 1b, displaying modes with dominant C≡N (2352 cm^{-1}) or C=C (1451 cm^{-1}) bond stretching. Some of the small wavenumber modes (<1400 cm^{-1}) have significant hybridization between different bond vibrations. The V−N label indicates modes with a significant component of V−N stretching bonds. In Figure 2, we plot an experimental Raman spectrum next to the DFT phonon density of states (DOS). Based on the comparison, we assign the experimental 1300−

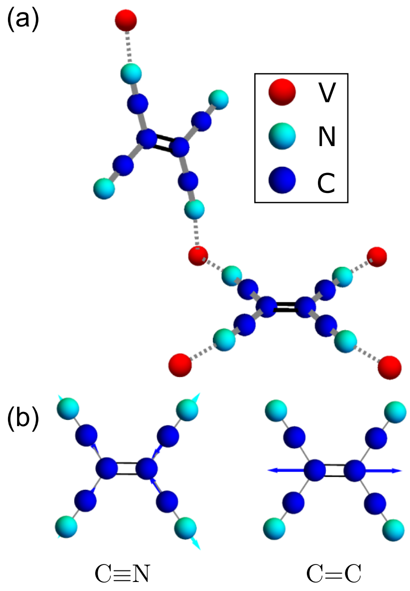

Figure 1. V[TCNE]$_x$ structure and vibrational modes based on density functional theory (DFT) calculations. (a) V[TCNE]$_x$ structure, showing two nonequivalent TCNE molecules. The bottom TCNE is bonded with four vanadium ions (μ4 bonded), while the top TCNE is bonded with two vanadium ions (trans-μ2 bonded). (b) DFT-calculated normal modes with dominant C≡N (2352 cm^{-1}) or C=C (1451 cm^{-1}) motion. Arrow lengths are proportional to the calculated vibration mode amplitudes. Some ions have motion too small to be seen on this scale. Shown is the bottom (μ4 bonded) TCNE. Because the two TCNE are nonequivalent, high wavenumber vibrational modes (>1000 cm^{-1}) are not hybridized and are localized on one or the other TCNE.

1500 cm^{-1} Raman peaks to C=C stretching modes and 2200 cm^{-1} Raman peaks to C≡N stretching modes.

Next, we analyze the Raman spectra in greater detail. Raman peaks near 2202 and 2225 cm^{-1} are in agreement with previous IR spectrum peaks at 2194 and 2214 cm^{-1}.[4,50] We observe a Raman peak at 2121 cm^{-1}, whereas previous IR spectra only had a peak at 2155 cm^{-1},[50] which could be explained by the IR and Raman activities of these vibrational modes. The Raman peaks at 1308, 1411, and 1530 cm^{-1} are absent in the IR spectrum, suggesting vanadium ions are more symmetrically bonded to the center C=C bond, leading to low IR activity.[4] While the peaks at 1308 and 1530 cm^{-1} are initially weak, as shown here, they grow substantially in aged and laser damaged samples. We attribute low wavenumber peaks at 336, 457, and 543 cm^{-1} to low-energy TCNE vibrational modes and V−N stretching modes. These low wavenumber modes are particularly relevant for magnetism, as they are influenced by V−N bonds.

Ferromagnetic Resonance. We next measure the effective magnetization of the V[TCNE]$_x$ film by angle-resolved FMR. The resonance frequency ω with an external field much greater than the effective magnetization of the material ($H \gg 4\pi M_{\rm eff}$) is[6]

$$\omega = \gamma\sqrt{(H - 4\pi M_{\rm eff}\cos^2\theta)(H - 4\pi M_{\rm eff}\cos 2\theta)} \qquad (1)$$

where γ is the gyromagnetic ratio, H is the external magnetic field, θ is the angle of the external field with respect to the film normal, $4\pi M_{\rm eff} = 4\pi M_{\rm S} - H_{\rm k}$, which is a combination of the saturation magnetization and the anisotropy field. One possible source of the anisotropy field is from strain due to the differential thermal expansion of V[TCNE]$_x$ and the underlying substrate.[21,62] In Figure 3, we show a field-modulated FMR signal measured at 3 GHz. Fitting the angle-resolved FMR data, we extract an effective field $4\pi M_{\rm eff}$ = 68 Oe. The

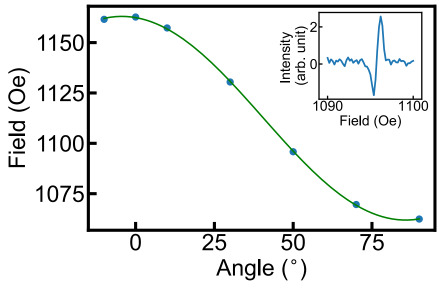

Figure 3. Angle-resolved FMR measured at 3 GHz microwave frequency. Fitted $4\pi M_{\rm eff}$ = 68 Oe. (Inset) Field sweep at 50°. Fitted FWHM linewidth is 1.1 Oe.

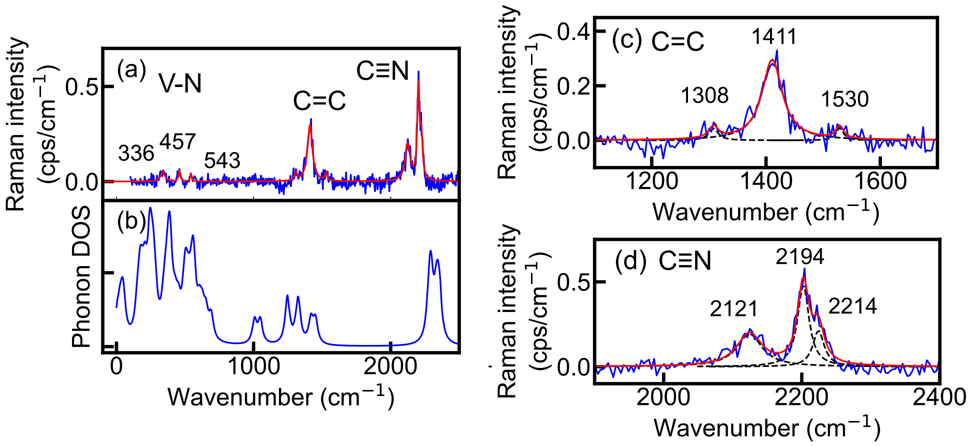

Figure 2. V[TCNE]$_x$ Raman spectra and density of states (DOS). (a) Experimental spectrum of pristine encapsulated V[TCNE]$_x$. A broad baseline is subtracted from the raw Raman spectrum (see Supporting Information, SI). Data (blue), fit (red). V−N modes at 336, 457, and 543 cm^{-1} (b) *Ab initio* V[TCNE]$_x$ phonon DOS. In the plot, each mode is broadened as a Lorentzian with a full width at half maximum (FWHM) of 20 cm^{-1}. (c) C=C. (d) C≡N modes. Individual Lorentzian fits (black, dashed). C=C 1308, 1411, and 1530 cm^{-1}. C≡N 2121, 2194, and 2214 cm^{-1}.

FWHM linewidth is 1.1 Oe, which is comparable to previously reported values.[20]

Photoluminescence and Laser Damage Susceptibility. Having characterized a pristine V[TCNE]$_x$ film, we turn our attention to V[TCNE] aging mechanisms. Here, we introduce aging by laser-induced damage to study aging in the absence of oxygen and water. There is also an independent interest in studying V[TCNE]$_x$ under focused laser illumination, in particular in relation to experiments coupling V[TCNE]$_x$ with defect centers.[31]

Here, we study Sample 2, a 1.6 μm thick V[TCNE]$_x$ film. We illuminate a given spot at varied but high optical power for 4 min and then collect Raman spectra with a constant and low laser power (93 μW) for 4 min. We then repeat this procedure using a different 'high' excitation power at an undamaged region of the sample.

We observe that photoluminescence increases under continuous illumination, and it is accompanied by a color change in the V[TCNE]$_x$ film. Because a color change is associated with a chemical change in V[TCNE]$_x$, we use photoluminescence (PL) as a proxy for aging and use the change in PL as a proxy for laser damage. Here, we consider a quantity that is insensitive to variation in the initial photoluminescence rate. We define laser damage susceptibility χ_{PL} as the fractional rate of change in photoluminescence per unit optical power, namely

$$\chi_{\mathrm{PL}} = \frac{1}{P_{\mathrm{opt}}} \frac{1}{\mathrm{PL}(t=0)} \frac{\mathrm{d}}{\mathrm{d}t} \mathrm{PL}(t) \tag{2}$$

where PL is the photoluminescence and P_{opt} is the incident laser power. This is defined to measure the laser damage rate per unit optical power. Note that if laser damage is a one-photon process, then the total damage is only a function of the total photon dose, in which case, χ_{PL} would be independent of laser power.

At a fixed power, PL gradually saturates in minutes to hours. As such, we linearly fit the initial photoluminescence increase (Figure 4a inset) and extract χ_{PL}. Laser damage susceptibility increases with optical power (Figure 4a), which indicates that at high optical power, laser damage is not a single photon process for laser wavelength 532 nm. Instead, this suggests laser damage is due to heating. While the temperature rise is proportional to laser power, chemical reaction rates increase nonlinearly with temperature, causing more rapid aging at a high optical power.

Next, we examine the Raman spectra in detail. After exposure to higher laser power, the Raman intensity near 2121 cm^{-1} decreases with a corresponding increase in the 2202 and 2225 cm^{-1} peaks (Figure 4b,d). The side peaks at 1308 and 1530 cm^{-1} associated with C═C bonds increase in intensity and linewidth (Figure 4b,c). The low wavenumber peaks (<600 cm^{-1}) disappear. In addition, the total fluorescence background increases with increasing laser power. The quantitative changes in Raman intensity are shown in Figure 4c,d. The disappearance of low wavenumber (<600 cm^{-1}) and the 2121 cm^{-1} Raman peaks are clear, qualitative signatures of film aging. Low wavenumber vibrational modes have significant V−N stretching components; therefore, the disappearance of those peaks suggests a reduction in vanadium bonding to TCNE groups. This may lead to a weaker spin−spin coupling and reduced magnetization. Likewise, the 2121 cm^{-1} Raman peak corresponds to C≡N vibrational modes, which are sensitive to vanadium nitrogen bonding and are therefore also relevant for magnetic ordering in V[TCNE]$_x$.

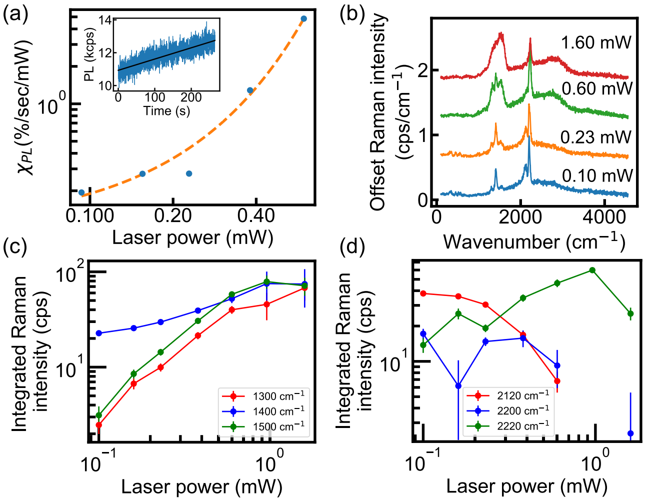

Figure 4. (a) Laser damage susceptibility χ_{PL} increases with optical power. Also shown is a guide to the eye showing an exponential dependence on power. Inset - photoluminescence time trace at an optical power 0.23 mW. (b) Raw Raman spectra taken at 0.10 mW after exposing to different powers of the laser for 4 min. (c), (d) Baseline-subtracted integrated Raman intensity around 1400 cm^{-1}. (d) Integrated Raman intensity around 2200 cm^{-1}.

Aging. Having characterized pristine encapsulated V[TCNE]$_x$ and laser-induced damage, we next study its aging at room temperature in ambient atmosphere. As V[TCNE]$_x$ ages, it turns from blue-black opaque to transparent, with a transparency front beginning at the sample edges and propagating under the glass coverslip (Figure 5a). We attribute this change to chemical reactions with diffused oxygen and water across the epoxy encapsulation barrier at the sample edges.

In contrast, V[TCNE]$_x$ far from the edges does not show a strong color change with time, suggesting it has not been oxidized. We therefore characterize photoluminescence and Raman spectra at the center of the sample. Raman spectra show an increase in the fluorescence background and an increase in the Raman intensity near 1300−1500 cm^{-1} over time (Figure 5b). In addition, peaks near 1300 and 1500 cm^{-1} increase in Raman intensity compared to the center 1400 cm^{-1} peak. Over a longer timescale (89 days), the low wavenumber peaks (336, 457, and 543 cm^{-1}) vanish, and the 2120 cm^{-1} peak further diminishes. These features are qualitatively similar to those observed in laser damaged samples, with the strongest changes appearing in V−N and C≡N bonding. This suggests that the slow processes present in room temperature aging are similar to the chemical reactions accelerated by laser damage.

A more drastic signature of aging is an increase in laser damage susceptibility χ_{PL}, which increases exponentially in time (Figure 5c). Concurrently, the effective magnetization $4\pi M_{\mathrm{eff}}$ decreases over time (Figure 5c). This establishes a link between the optical properties and magnetic properties, indicating optical measurement is a local probe of V[TCNE]$_x$ film quality.

To better understand long-term aging, we examine two other V[TCNE]$_x$ samples. One is a 4-year-old uniform film (sample 5), and the other is a 2-year-old, patterned film with 100 μm wide bars (sample 6). Both of them are nominally 1

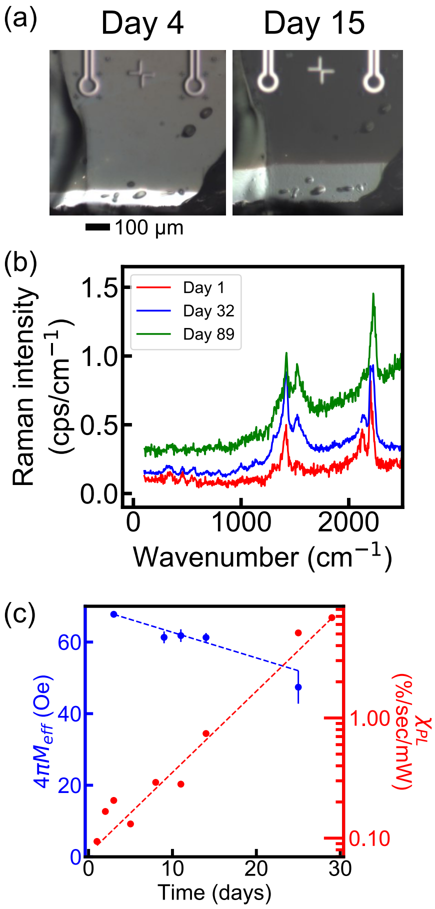

Figure 5. (a) Visual indication of $\mathrm{V[TCNE]}_x$ aging, showing the aging front advancing from day 4 to day 15. The $\mathrm{V[TCNE]}_x$ film turns transparent and reveals the underlying reflective aluminum layer. (b) Raman spectrum without baseline subtraction on day 1 (red), day 32 (blue), and day 89 (green) near the sample center. The overall fluorescence/Raman background floor increases and peaks at 1300, 1500 cm^{-1} increases. Over long time (89 days), low wavenumber peaks (300−600 cm^{-1}) and the peak near 2120 cm^{-1} vanish. (c) Reduction in $4\pi M_{\mathrm{eff}}$ and an increase in laser damage susceptibility. Laser damage susceptibility measured at the center of the sample, using a laser power of 100−200 μW. Fitted lines decay rate is 0.72 Oe/day, and laser damage susceptibility increases with a $1/e$ time constant of 6.4 days.

μm thick, estimated from the growth time. Both of them are visually opaque and yet are magnetically inactive.

First, we measure Raman spectra with a low laser power. As we collect the spectra, we raster scan across the sample to minimize laser damage and ensure we are measuring only the effects of aging. The samples show qualitatively similar Raman peaks (Figure 6d−f), with three peaks near 1300−1500 cm^{-1} and a single peak near 2200 cm^{-1}. In particular, the center 1400 cm^{-1} peak is sharp and spectrally resolved from the 1300 and 1500 cm^{-1} peaks. There is a small residue of the 2120 cm^{-1} peak in the 89 day sample (Figure 6f), indicating incomplete aging.

Next, we study the effects of laser damage on aged samples. Under strong laser illumination, three peaks 1300−1500 cm^{-1} merge into two broad peaks and become brighter than the 2200 cm^{-1} peak, which is similar to laser damage in a pristine sample (Figure 4b). Low wavenumber peaks (300−600 cm^{-1}, V−N) and the 2120 cm^{-1} peak (C≡N) are absent or significantly reduced in thoroughly aged samples, further supporting a link between these Raman features and good magnetic properties. The above changes in Raman spectra are consistent with recent electron energy-loss spectroscopy (EELS) results,[63] which suggests a change in vanadium coordination with nitrogen and a change from C═C to C−C bonds in aged and oxidized samples.

The detailed mechanism of laser damage remains unclear. One may speculate that one mechanism is the release of oxygen from the epoxy under intense laser illumination, leading to oxidation of the sample. However, laser damage is similar across all samples, including Sample 1, where the $\mathrm{V[TCNE]}_x$ film is encapsulated with a 73 nm aluminum layer and thus is not in direct contact with the epoxy. Indeed, aluminum would provide an effective oxidation barrier. We note that the estimated temperature of $\mathrm{V[TCNE]}_x$ under damaging laser intensities is higher than the growth temperature, which could decompose $\mathrm{V[TCNE]}_x$ even in the absence of oxygen. Although more than one mechanism could be at work, a detailed understanding is beyond the scope of this article and a topic for future study.

One limitation of the above angle-resolved FMR is that it only measures an intensive quantity, M_{eff}. To understand the change in the magnetic moment, we monitor the aging of another 400 nm thick $\mathrm{V[TCNE]}_x$ film (sample 3) with SQUID magnetometry and FMR. We compare three quantities, total magnetic moment m_{tot} measured by SQUID magnetometry, effective magnetization ($4\pi M_{\mathrm{eff}}$), and weighted total moment m_{w} measured by angle-resolved FMR, which we define in the following paragraphs. Since m_{tot} and m_{w} are extensive quantities while $4\pi M_{\mathrm{eff}}$ is an intensive quantity, we explain below in detail the measurement procedure for each quantity and how we compare them.

We compute the saturation magnetization $4\pi M_{\mathrm{S}}$ from SQUID magnetometry data by normalizing the total moment to the $\mathrm{V[TCNE]}_x$ film volume. The volume has an uncertainty of up to 20%, which is dominated by the thickness uncertainty. This study lacks a direct measure of the sample thickness for each sample, and there are growth-to-growth variations in the growth rate as well as variations of the growth rate across different positions in the growth chamber. Nonetheless, we are most interested in how M_{S} changes in the aging process, which is less dependent on the initial sample volume. We also note that the volume of ferrimagnetic $\mathrm{V[TCNE]}_x$ is not constant, as the sample ages due to the oxidation front that propagates from the sample edge to center (see Figure 5a), resulting in a 33% reduction in the opaque area over 32 days. In Figure 7b, we plot the moment normalized to the initial $\mathrm{V[TCNE]}_x$ volume. We denote this quantity as $4\pi M_{\mathrm{S}}$, and we interpret it as a scaled total ferrimagnetic moment.

Next, we discuss FMR measurements. We note that the sample has a low loss fraction throughout the course of the experiment, with a Gilbert damping α that varies from 1.5 to 2.5×10^{-4} from day 1 to day 20 (Figure 7a). The Gilbert damping is extracted from a least-squares fit of the linewidth as a function of frequency. The error bars are calculated from the uncertainty of the fit, which does not capture all sources of uncertainty. We can unambiguously detect a resonance line shape and the typical uncertainty in $4\pi M_{\mathrm{eff}}$ is ~1 Oe. Because we measure FMR with field modulation, we are insensitive to high damping magnetic material, which will appear as a broad background.

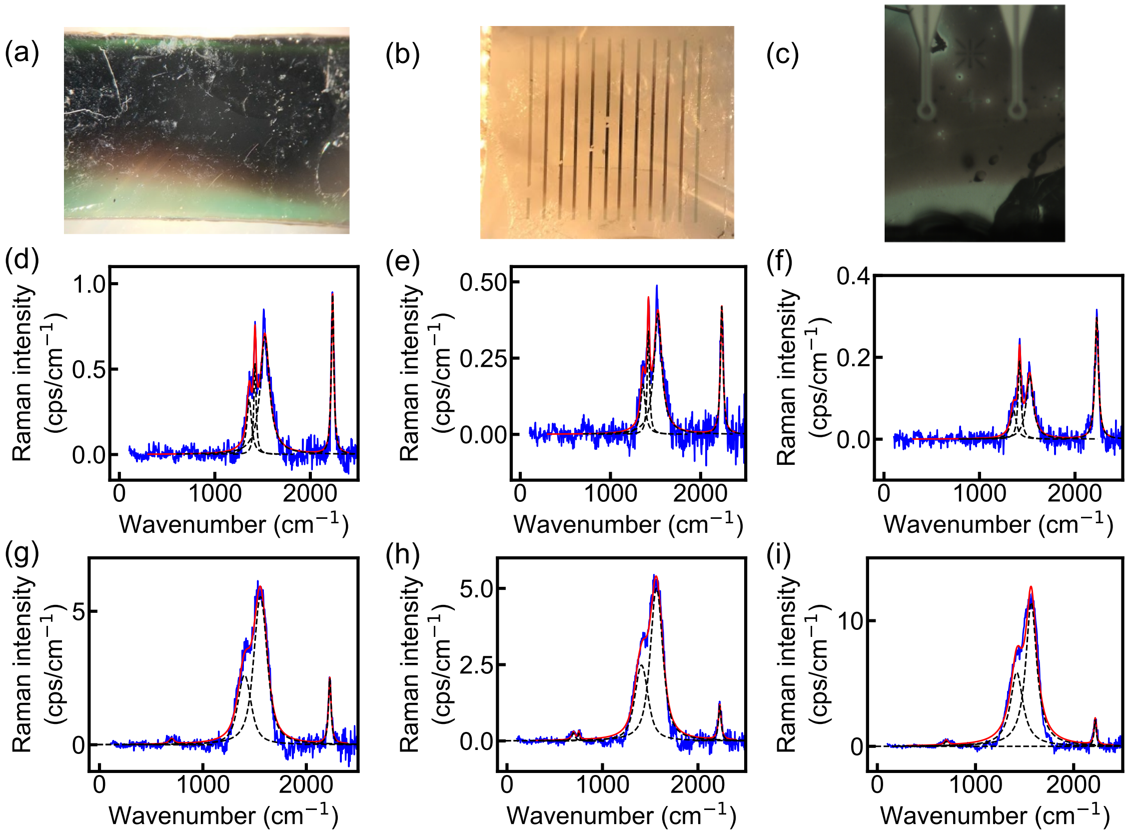

Figure 6. Long-term study of encapsulated V[TCNE]$_x$. The Raman spectra are baseline subtracted. We probe the center opaque areas away from encapsulation edges in all three samples. (a), (d), and (g) (sample 5) 4-year-old, 1 μm thick uniform film. (b), (e), and (h) (sample 6) 2-year-old, 1 μm thick, patterned film with 100 μm wide bar sample. (c), (f), and (i) (sample 1 in the main text) 89-day-old, 400 nm thick film with aluminum encapsulation. Note that the V[TCNE]$_x$ film has been remounted on the antenna and their relative positions differ from that in Figure 5. (d)−(f) Raman spectra (blue), fit (red), and individual Lorentzian fit (black dashed). The laser power is reduced, and the laser spot is raster scanned across near a 50 μm^2 area such that the samples undergo negligible damage during measurement. The laser power is (d) 190 μW, (e) 190 μW, and (f) 51 μW. (g)−(i) We increase the laser power and focus on a single spot to evaluate the effects of laser damage. The laser power used is 1.9 mW.

This weighted moment m_w is computed based on FMR signal amplitude. We fit for a sum of absorption derivative line shape $L'_{\mathrm{abs}}(H) = a\frac{\Delta H^3(H-H_0)}{(\Delta H^2+4(H-H_0)^2)^2}$ and dispersive derivative line shape $L'_{\mathrm{disp}}(H) = d\frac{\Delta H^2(\Delta H^2-4(H-H_0)^2)}{(\Delta H^2+4(H-H_0)^2)^2}$, where a and d are the amplitudes, H_0 is the resonance field, and ΔH is the full-width-half-max linewidth. We estimate the magnetic moment using the product of signal amplitude and FWHM $a\Delta H$. This quantity is analogous to the double integrated signal in FMR.[64,65] We normalize $a\Delta H$ to the microwave power and the modulation amplitude (see SI) to compute m_w, which is proportional to the magnetic moment. Because the sample (width = 2450 μm) is several times wider than the microwave waveguide (width = 430 μm), the FMR sensitivity is nonuniform across the sample. Hence we note m_w is a measure of the weighted magnetic moment and is more sensitive to the sample portion closer to the microwave waveguide. Moreover, the sample has been remounted multiple times as we alternate between the SQUID and FMR setups, so the coupling between the V[TCNE]$_x$ film and the microwave waveguide varies. With the above subtleties pointed out, we use FMR intensity m_w to estimate the weighted magnetic moment with low damping.

Over the course of the study (38 days), $4\pi M_S$ and m_w reduce by nearly 2 orders of magnitude (Figure 7b). In comparison, $4\pi M_{\mathrm{eff}}$ only changes from 95 ± 2 to 45 ± 1 Oe. These findings suggest an aging process, where the magnetic portion shrinks, resulting in the large decrease in the total moment. However, the remaining portion has low damping and a reduction of M_{eff} within a factor of 2. Over the first 20 days, the Gilbert damping α varies non-monotonically by a factor of 1.6, whereas $4\pi M_{\mathrm{eff}}$ reduces monotonically by a factor of 1.8 and m_w reduces by a factor of 10. Together with a lack of a clear trend in the Gilbert damping, we conclude that α remains essentially constant, and there are other sources of uncertainty, in addition to the model fit uncertainty. This is consistent with an aging front propagating from the sample edge to center, where the center is relatively pristine. These measurements suggest intrinsic aging due to internal chemical reaction at room temperature does not increase damping significantly for at least 20 days.

Laser Patterning. With the understanding of how V[TCNE]$_x$ ages naturally and via laser heating, we next explore how to use this knowledge for magnetic patterning. Instead of merely being a nuisance, laser damage could also be used for patterning with micron-scale spatial extent by selectively removing magnetism. We show a proof-of-concept demonstration by laser patterning the authors' affiliations on a V[TCNE]$_x$ film (Figure 8a), where the laser-written area is

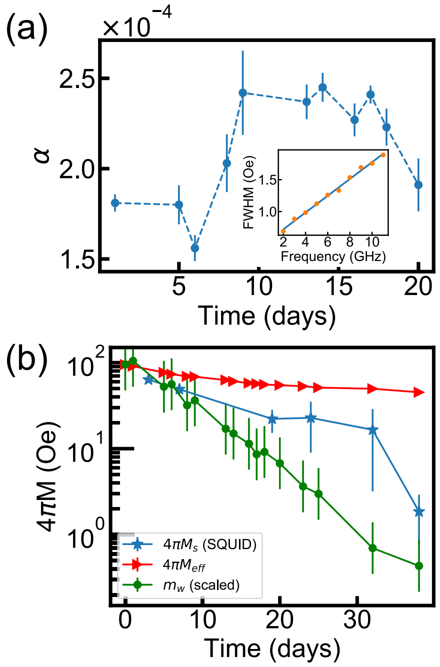

Figure 7. Magnetic properties of an encapsulated V[TCNE]$_x$ film (sample 3) as it ages at room temperature. (a) The Gilbert damping parameter α extracted from FMR measurements in the range 2−11 GHz, with an out-of-plane static magnetic field. (Inset) Gilbert damping fit on day 1. α = (1.8 ± 0.1) × 10^{-4}. (b) Magnetic measurements vs sample aging time. SQUID magnetometry measurements and FMR intensity consistently show a large decrease in magnetic moment. m_w data is scaled such that it equals $4\pi M_{eff}$ on the first day of measurement. In comparison, $4\pi M_{eff}$ shows a much smaller change over the same period of time.

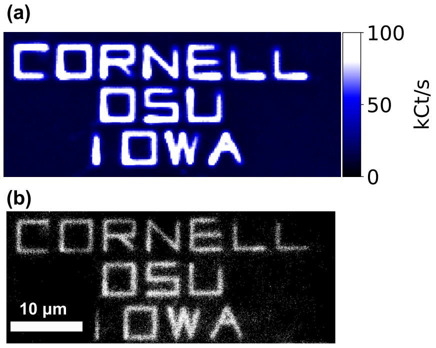

Figure 8. Laser patterning of a 400 nm thick V[TCNE]$_x$ sample (sample 4). (a) Photoluminescence map. High count rate regions are laser damaged, low count rate regions are the remaining undamaged material. (b) Grayscale optical micrograph of the same area. Laser damaged areas are more transparent and appear brighter in the image. This is patterned with 1.7 mW laser power, corresponding to an optical intensity of 1.3 × 10^6 W/cm^2.

damaged, producing much higher photoluminescence. Laser patterned feature size is on the order of 1 μm based on the photoluminescence map. The magnetic properties of laser patterned samples, e.g., the magnetization profile and the supported spin-wave modes, will be topics of future study.

■ CONCLUSIONS

We characterize pristine encapsulated V[TCNE]$_x$ thin films using confocal microscopy, micro-focused Raman spectroscopy, FMR, and SQUID magnetometry. Through comparison with *ab initio* calculations, we associate the experimentally observed Raman peaks with particular C≡N, C=C stretching modes. We measure how the sample photoluminescence depends on laser power and observe that laser damage susceptibility increases with laser power. This is consistent with a heating-based laser damage mechanism, where chemical reaction rate increases nonlinearly with temperature.

We identify changes in Raman spectra and laser damage susceptibility as the sample ages. Small wavenumber (300−600 cm^{-1}) Raman features associated with V−N bonds vanish as the sample ages, suggesting changes in bonding between vanadium and TCNE. Changes in C=C (1300−1500 cm^{-1}) and C≡N (2100−2220 cm^{-1}) Raman peaks indicate structural changes in TCNE. These findings show that optical measurement is a local probe of V[TCNE]$_x$ film magnetic quality and could assess magnetic microstructure quality. We further explore laser damage as a means of patterning and perform a proof-of-concept demonstration.

The existence of a narrow FMR response in encapsulated V[TCNE]$_x$ films for at least 20 days at room temperature suggests that intrinsic aging (e.g., not oxidation) does not increase damping significantly over this time interval. This is promising for coherent magnonics using V[TCNE]$_x$ microstructures that are positioned far from encapsulation edges. For quantum applications that use V[TCNE]$_x$ at cryogenic temperatures, the damping properties are expected to be preserved over an even longer timescale.

■ ASSOCIATED CONTENT

Supporting Information

The Supporting Information is available free of charge at https://pubs.acs.org/doi/10.1021/acs.jpcc.1c04582.

Confocal measurements, Raman spectroscopy, *ab initio* calculations, ferromagnetic resonance, FMR data analysis, laser heating, and SQUID magnetometry (PDF)

■ AUTHOR INFORMATION

Corresponding Author

Gregory D. Fuchs − *School of Applied and Engineering Physics, Cornell University, Ithaca, New York 14853, United States; Kavli Institute at Cornell for Nanoscale Science, Ithaca, New York 14853, United States;* orcid.org/0000-0003-4343-8523; Email: gdf9@cornell.edu

Authors

Hil Fung Harry Cheung − *School of Applied and Engineering Physics, Cornell University, Ithaca, New York 14853, United States*

Michael Chilcote − *School of Applied and Engineering Physics, Cornell University, Ithaca, New York 14853, United States*

Huma Yusuf − *Department of Physics, The Ohio State University, Columbus, Ohio 43210, United States*

Donley S. Cormode − *Department of Physics, The Ohio State University, Columbus, Ohio 43210, United States*

Yueguang Shi − *Department of Physics and Astronomy, University of Iowa, Iowa City, Iowa 52242, United States*

Seth Kurfman − *Department of Physics, The Ohio State University, Columbus, Ohio 43210, United States*

Andrew Franson − *Department of Physics, The Ohio State University, Columbus, Ohio 43210, United States*

Michael E. Flatté − *Department of Physics and Astronomy, University of Iowa, Iowa City, Iowa 52242, United States; Department of Applied Physics, Eindhoven University of Technology, Eindhoven 5612 AZ, The Netherlands;* orcid.org/0000-0001-5093-1549

Ezekiel Johnston-Halperin − *Department of Physics, The Ohio State University, Columbus, Ohio 43210, United States;* orcid.org/0000-0002-6240-3505

Complete contact information is available at: https://pubs.acs.org/10.1021/acs.jpcc.1c04582

Notes

The authors declare no competing financial interest.

■ ACKNOWLEDGMENTS

Optical Raman experiments, optical writing experiments, waveguide FMR studies of aging, first-principles theory, and sample growth of aging study samples were supported by the US Department of Energy, Office of Science, Office of Basic Energy Sciences under Award DE-SC0019250. Control sample growth and cavity FMR characterization, as well as growth of 2−4-year-old samples were supported by NSF DMR-1808704 and DMR-1507775. The authors acknowledge use of the facilities of the Cornell Center for Materials Research, which is supported through the NSF MRSEC program (DMR-1719875), and the Cornell NanoScale Facility, which is a member of the National Nanotechnology Coordinated Infrastructure and supported by the NSF (NNCI-2025233). The authors acknowledge helpful discussions with Brendan McCullian. The authors thank Hong Tang and Na Zhu for providing 2−4 year old V[TCNE]$_x$ reference samples.

■ REFERENCES

(1) Awschalom, D. D.; Du, C. H. R.; He, R.; Heremans, J.; Hoffmann, A.; Hou, J.; Kurebayashi, H.; Li, Y.; Liu, L.; Novosad, V.; et al. Quantum Engineering With Hybrid Magnonics Systems and Materials. IEEE Transactions on Quantum Engineering. *IEEE Trans. Quantum Eng.* **2021**, 1.

(2) Manriquez, J. M.; Yee, G. T.; Mclean, R. S.; Epstein, A. J.; Miller, J. S. A Room-Temperature Molecular/Organic-Based Magnet. *Science* **1991**, *252*, 1415−1417.

(3) Miller, J. S.; Epstein, A. J. Tetracyanoethylene-Based Organic Magnets. *Chem. Commun.* **1998**, *1998*, 1319−1325.

(4) Pokhodnya, K. I.; Epstein, A. J.; Miller, J. S. Thin-Film V[TCNE]x Magnets. *Adv. Mater.* **2000**, *12*, 410−413.

(5) Plachy, R.; Pokhodnya, K. I.; Taylor, P. C.; Shi, J.; Miller, J. S.; Epstein, A. J. Ferrimagnetic Resonance in Films of Vanadium [Tetracyanoethanide]$_x$, Grown by Chemical Vapor Deposition. *Phys. Rev. B* **2004**, *70*, No. 064411.

(6) Yu, H.; Harberts, M.; Adur, R.; Lu, Y.; Hammel, P. C.; Johnston-Halperin, E.; Epstein, A. J. Ultra-Narrow Ferromagnetic Resonance in Organic-Based Thin Films Grown via Low Temperature Chemical Vapor Deposition. *Appl. Phys. Lett.* **2014**, *105*, No. 012407.

(7) Liu, H.; Zhang, C.; Malissa, H.; Groesbeck, M.; Kavand, M.; McLaughlin, R.; Jamali, S.; Hao, J.; Sun, D.; Davidson, R. A.; et al. Organic-Based Magnon Spintronics. *Nat. Mater.* **2018**, *17*, 308−312.

(8) Liu, H.; Malissa, H.; Stolley, R. M.; Singh, J.; Groesbeck, M.; Popli, H.; Kavand, M.; Chong, S. K.; Deshpande, V. V.; Miller, J. S.; et al. Spin Wave Excitation, Detection, and Utilization in the Organic-Based Magnet, V(TCNE)$_x$ (TCNE = Tetracyanoethylene). *Adv. Mater.* **2020**, *32*, No. 2002663.

(9) Tabuchi, Y.; Ishino, S.; Noguchi, A.; Ishikawa, T.; Yamazaki, R.; Usami, K.; Nakamura, Y. Coherent Coupling between a Ferromagnetic Magnon and a Superconducting Qubit. *Science* **2015**, *349*, 405−408.

(10) Huebl, H.; Zollitsch, C. W.; Lotze, J.; Hocke, F.; Greifenstein, M.; Marx, A.; Gross, R.; Goennenwein, S. T. B. High Cooperativity in Coupled Microwave Resonator Ferrimagnetic Insulator Hybrids. *Phys. Rev. Lett.* **2013**, *111*, No. 127003.

(11) Wang, Y.-P.; Rao, J. W.; Yang, Y.; Xu, P.-C.; Gui, Y. S.; Yao, B. M.; You, J. Q.; Hu, C.-M. Nonreciprocity and Unidirectional Invisibility in Cavity Magnonics. *Phys. Rev. Lett.* **2019**, *123*, No. 127202.

(12) McKenzie-Sell, L.; Xie, J.; Lee, C.-M.; Robinson, J. W. A.; Ciccarelli, C.; Haigh, J. A. Low-Impedance Superconducting Microwave Resonators for Strong Coupling to Small Magnetic Mode Volumes. *Phys. Rev. B* **2019**, *99*, No. 140414.

(13) Wolski, S. P.; Lachance-Quirion, D.; Tabuchi, Y.; Kono, S.; Noguchi, A.; Usami, K.; Nakamura, Y. Dissipation-Based Quantum Sensing of Magnons with a Superconducting Qubit. *Phys. Rev. Lett.* **2020**, *125*, No. 117701.

(14) Lachance-Quirion, D.; Tabuchi, Y.; Gloppe, A.; Usami, K.; Nakamura, Y. Hybrid Quantum Systems Based on Magnonics. *Appl. Phys. Express* **2019**, *12*, No. 070101.

(15) Lachance-Quirion, D.; Wolski, S. P.; Tabuchi, Y.; Kono, S.; Usami, K.; Nakamura, Y. Entanglement-Based Single-Shot Detection of a Single Magnon with a Superconducting Qubit. *Science* **2020**, *367*, 425−428.

(16) Hauser, C.; Richter, T.; Homonnay, N.; Eisenschmidt, C.; Qaid, M.; Deniz, H.; Hesse, D.; Sawicki, M.; Ebbinghaus, S. G.; Schmidt, G. Yttrium Iron Garnet Thin Films with Very Low Damping Obtained by Recrystallization of Amorphous Material. *Sci. Rep.* **2016**, *6*, No. 20827.

(17) Sun, Y.; Song, Y.-Y.; Chang, H.; Kabatek, M.; Jantz, M.; Schneider, W.; Wu, M.; Schultheiss, H.; Hoffmann, A. Growth and Ferromagnetic Resonance Properties of Nanometer-Thick Yttrium Iron Garnet Films. *Appl. Phys. Lett.* **2012**, *101*, No. 152405.

(18) Liu, T.; Chang, H.; Vlaminck, V.; Sun, Y.; Kabatek, M.; Hoffmann, A.; Deng, L.; Wu, M. Ferromagnetic Resonance of Sputtered Yttrium Iron Garnet Nanometer Films. *J. Appl. Phys.* **2014**, *115*, No. 17A501.

(19) Zhu, N.; Zhang, X.; Froning, I. H.; Flatté, M. E.; Johnston-Halperin, E.; Tang, H. X. Low Loss Spin Wave Resonances in Organic-Based Ferrimagnet Vanadium Tetracyanoethylene Thin Films. *Appl. Phys. Lett.* **2016**, *109*, No. 082402.

(20) Franson, A.; Zhu, N.; Kurfman, S.; Chilcote, M.; Candido, D. R.; Buchanan, K. S.; Flatté, M. E.; Tang, H. X.; Johnston-Halperin, E. Low-Damping Ferromagnetic Resonance in Electron-Beam Patterned, High-Q Vanadium Tetracyanoethylene Magnon Cavities. *APL Mater.* **2019**, *7*, No. 121113.

(21) Yusuf, H.; Chilcote, M.; Candido, D. R.; Kurfman, S.; Cormode, D. S.; Lu, Y.; Flatté, M. E.; Johnston-Halperin, E. Exploring a Quantum-Information-Relevant Magnonic Material: Ultralow Damping at Low Temperature in the Organic Ferrimagnet V[TCNE]x. *AVS Quantum Sci.* **2021**, *3*, No. 026801.

(22) Bai, L.; Harder, M.; Chen, Y. P.; Fan, X.; Xiao, J. Q.; Hu, C.-M. Spin Pumping in Electrodynamically Coupled Magnon-Photon Systems. *Phys. Rev. Lett.* **2015**, *114*, No. 227201.

(23) Harder, M.; Yang, Y.; Yao, B. M.; Yu, C. H.; Rao, J. W.; Gui, Y. S.; Stamps, R. L.; Hu, C.-M. Level Attraction Due to Dissipative Magnon-Photon Coupling. *Phys. Rev. Lett.* **2018**, *121*, No. 137203.

(24) Haigh, J. A.; Lambert, N. J.; Doherty, A. C.; Ferguson, A. J. Dispersive Readout of Ferromagnetic Resonance for Strongly Coupled Magnons and Microwave Photons. *Phys. Rev. B* **2015**, *91*, No. 104410.

(25) Zhu, N.; Zhang, X.; Han, X.; Zou, C.-L.; Zhong, C.; Wang, C.-H.; Jiang, L.; Tang, H. X. Waveguide Cavity Optomagnonics for Microwave-to-Optics Conversion. *Optica* **2020**, *7*, 1291−1297.

(26) Zhang, X.; Zhu, N.; Zou, C.-L.; Tang, H. X. Optomagnonic Whispering Gallery Microresonators. *Phys. Rev. Lett.* **2016**, *117*, No. 123605.

(27) Parvini, T. S.; Bittencourt, V. A. S. V.; Kusminskiy, S. V. Antiferromagnetic Cavity Optomagnonics. *Phys. Rev. Res.* **2020**, *2*, No. 022027.

(28) Graf, J.; Pfeifer, H.; Marquardt, F.; Viola Kusminskiy, S. Cavity Optomagnonics with Magnetic Textures: Coupling a Magnetic Vortex to Light. *Phys. Rev. B* **2018**, *98*, No. 241406.

(29) van der Sar, T.; Casola, F.; Walsworth, R.; Yacoby, A. Nanometre-Scale Probing of Spin Waves Using Single Electron Spins. *Nat. Commun.* **2015**, *6*, No. 7886.

(30) Andrich, P.; de las Casas, C. F.; Liu, X.; Bretscher, H. L.; Berman, J. R.; Heremans, F. J.; Nealey, P. F.; Awschalom, D. D. Long-Range Spin Wave Mediated Control of Defect Qubits in Nanodiamonds. *npj Quantum Inf.* **2017**, *3*, No. 28.

(31) Candido, D. R.; Fuchs, G. D.; Johnston-Halperin, E.; Flatté, M. E. Predicted Strong Coupling of Solid-State Spins Via a Single Magnon Mode. *Mater. Quantum Technol.* **2020**, *1*, No. 011001.

(32) Bertelli, I.; Carmiggelt, J. J.; Yu, T.; Simon, B. G.; Pothoven, C. C.; Bauer, G. E. W.; Blanter, Y. M.; Aarts, J.; van der Sar, T. Magnetic Resonance Imaging of Spin-Wave Transport and Interference in a Magnetic Insulator. *Sci. Adv.* **2020**, *6*, No. eabd3556.

(33) Trifunovic, L.; Pedrocchi, F. L.; Loss, D. Long-Distance Entanglement of Spin Qubits via Ferromagnet. *Phys. Rev. X* **2013**, *3*, No. 041023.

(34) Fukami, M.; Candido, D. R.; Awschalom, D. D.; Flatté, M. E. Opportunities for Long-Range Magnon-Mediated Entanglement of Spin Qubits via On- and Off-Resonant Coupling. 2021, arXiv:2101.09220. arXiv.org e-Print archive. https://arxiv.org/abs/2101.09220.

(35) Nava Antonio, G.; Bertelli, I.; Simon, B. G.; Medapalli, R.; Afanasiev, D.; van der Sar, T. Magnetic Imaging and Statistical Analysis of the Metamagnetic Phase Transition of FeRh with Electron Spins in Diamond. *J. Appl. Phys.* **2021**, *129*, No. 223904.

(36) Neuman, T.; Wang, D. S.; Narang, P. Nanomagnonic Cavities for Strong Spin-Magnon Coupling and Magnon-Mediated Spin-Spin Interactions. *Phys. Rev. Lett.* **2020**, *125*, No. 247702.

(37) Cao, Y.; Yan, P.; Huebl, H.; Goennenwein, S. T. B.; Bauer, G. E. W. Exchange Magnon-Polaritons in Microwave Cavities. *Phys. Rev. B* **2015**, *91*, No. 094423.

(38) Hahn, C.; Naletov, V. V.; de Loubens, G.; Klein, O.; d'Allivy Kelly, O.; Anane, A.; Bernard, R.; Jacquet, E.; Bortolotti, P.; Cros, V.; et al. Measurement of the Intrinsic Damping Constant in Individual Nanodisks of $Y_3Fe_5O_{12}$ and $Y_3Fe_5O_{12}$|Pt. *Appl. Phys. Lett.* **2014**, *104*, No. 152410.

(39) Jungfleisch, M. B.; Zhang, W.; Jiang, W.; Chang, H.; Sklenar, J.; Wu, S. M.; Pearson, J. E.; Bhattacharya, A.; Ketterson, J. B.; Wu, M.; et al. Spin waves in Micro-Structured Yttrium Iron Garnet Nanometer-Thick Films. *J. Appl. Phys.* **2015**, *117*, No. 17D128.

(40) Li, S.; Zhang, W.; Ding, J.; Pearson, J. E.; Novosad, V.; Hoffmann, A. Epitaxial Patterning of Nanometer-Thick $Y_3Fe_5O_{12}$ films with Low Magnetic Damping. *Nanoscale* **2016**, *8*, 388−394.

(41) Zhu, N.; Chang, H.; Franson, A.; Liu, T.; Zhang, X.; Johnston-Halperin, E.; Wu, M.; Tang, H. X. Patterned Growth of Crystalline $Y_3Fe_5O_{12}$ Nanostructures with Engineered Magnetic Shape Anisotropy. *Appl. Phys. Lett.* **2017**, *110*, No. 252401.

(42) Krysztofik, A.; Coy, L. E.; Kuświk, P.; Załeski, K.; Głowiński, H.; Dubowik, J. Ultra-Low Damping in Lift-off Structured Yttrium Iron Garnet Thin Films. *Appl. Phys. Lett.* **2017**, *111*, No. 192404.

(43) Jermain, C. L.; Aradhya, S. V.; Reynolds, N. D.; Buhrman, R. A.; Brangham, J. T.; Page, M. R.; Hammel, P. C.; Yang, F. Y.; Ralph, D. C. Increased Low-Temperature Damping in Yttrium Iron Garnet Thin Films. *Phys. Rev. B* **2017**, *95*, No. 174411.

(44) Tabuchi, Y.; Ishino, S.; Ishikawa, T.; Yamazaki, R.; Usami, K.; Nakamura, Y. Hybridizing Ferromagnetic Magnons and Microwave Photons in the Quantum Limit. *Phys. Rev. Lett.* **2014**, *113*, No. 083603.

(45) Kosen, S.; van Loo, A. F.; Bozhko, D. A.; Mihalceanu, L.; Karenowska, A. D. Microwave Magnon Damping in YIG Films at Millikelvin Temperatures. *APL Mater.* **2019**, *7*, No. 101120.

(46) Choi, M.-C.; Kim, Y.; Ha, C.-S. Polymers for Flexible Displays: From Material Selection to Device Applications. *Prog. Polym. Sci.* **2008**, *33*, 581−630.

(47) Chwang, A. B.; Rothman, M. A.; Mao, S. Y.; Hewitt, R. H.; Weaver, M. S.; Silvernail, J. A.; Rajan, K.; Hack, M.; Brown, J. J.; Chu, X.; et al. Thin Film Encapsulated Flexible Organic Electroluminescent Displays. *Appl. Phys. Lett.* **2003**, *83*, 413−415.

(48) Subbarao, S. P.; Bahlke, M. E.; Kymissis, I. Laboratory Thin-Film Encapsulation of Air-Sensitive Organic Semiconductor Devices. *IEEE Trans. Electron Devices* **2010**, *57*, 153−156.

(49) Grover, R.; Srivastava, R.; Rana, O.; Mehta, D. S.; Kamalasanan, M. N. New Organic Thin-Film Encapsulation for Organic Light Emitting Diodes. *J. Encapsulation Adsorpt. Sci.* **2011**, *01*, 23−28.

(50) Froning, I. H.; Harberts, M.; Lu, Y.; Yu, H.; Epstein, A. J.; Johnston-Halperin, E. Thin-Film Encapsulation of the Air-Sensitive Organic-Based Ferrimagnet Vanadium Tetracyanoethylene. *Appl. Phys. Lett.* **2015**, *106*, No. 122403.

(51) Kresse, G.; Furthmüller, J. Efficient Iterative Schemes for Ab Initio Total-Energy Calculations Using a Plane-Wave Basis Set. *Phys. Rev. B* **1996**, *54*, 11169−11186.

(52) Kresse, G.; Furthmüller, J. Efficiency of *Ab-Initio* Total Energy Calculations for Metals and Semiconductors Using a Plane-Wave Basis Set. *Comput. Mater. Sci.* **1996**, *6*, 15−50.

(53) Kresse, G.; Hafner, J. *Ab Initio* Molecular Dynamics for Liquid Metals. *Phys. Rev. B* **1993**, *47*, 558−561.

(54) Kresse, G.; Hafner, J. *Ab Initio* Molecular-Dynamics Simulation of the Liquid-Metal−Amorphous-Semiconductor Transition in Germanium. *Phys. Rev. B* **1994**, *49*, 14251−14269.

(55) Perdew, J. P.; Burke, K.; Ernzerhof, M. Generalized Gradient Approximation Made Simple. *Phys. Rev. Lett.* **1996**, *77*, 3865−3868.

(56) Cococcioni, M.; de Gironcoli, S. Linear Response Approach to the Calculation of the Effective Interaction Parameters in the LDA + U Method. *Phys. Rev. B* **2005**, *71*, No. 035105.

(57) Heyd, J.; Scuseria, G. E.; Ernzerhof, M. Hybrid Functionals Based on a Screened Coulomb Potential. *J. Chem. Phys.* **2003**, *118*, 8207−8215.

(58) De Fusco, G. C.; Pisani, L.; Montanari, B.; Harrison, N. M. Density Functional Study of the Magnetic Coupling in $V(TCNE)_2$. *Phys. Rev. B* **2009**, *79*, No. 085201.

(59) Cimpoesu, F.; Frecus, B.; Oprea, C. I.; Panait, P.; Gîrţu, M. A. Disorder, Exchange and Magnetic Anisotropy in the Room-Temperature Molecular Magnet V[TCNE]x - A Theoretical Study. *Comput. Mater. Sci.* **2014**, *91*, 320−328.

(60) Frecus, B.; Oprea, C. I.; Panait, P.; Ferbinteanu, M.; Cimpoesu, F.; Gîrţu, M. A. *Ab Initio* Study of Exchange Coupling for the Consistent Understanding of the Magnetic Ordering at Room Temperature in V[TCNE]x. *Theor. Chem. Acc.* **2014**, *133*, No. 1470.

(61) Haskel, D.; Islam, Z.; Lang, J.; Kmety, C.; Srajer, G.; Pokhodnya, K. I.; Epstein, A. J.; Miller, J. S. Local Structural Order in the Disordered Vanadium Tetracyanoethylene Room-Temperature Molecule-Based Magnet. *Phys. Rev. B* **2004**, *70*, No. 054422.

(62) Chilcote, M.; Harberts, M.; Fuhrmann, B.; Lehmann, K.; Lu, Y.; Franson, A.; Yu, H.; Zhu, N.; Tang, H.; Schmidt, G.; et al. Spin-Wave Confinement and Coupling in Organic-Based Magnetic Nanostructures. *APL Mater.* **2019**, *7*, No. 111108.

(63) Trout, A.; Kurfman, S.; Chilcote, M.; Johnston-Halperin, E.; McComb, D. Electron Energy Loss Spectroscopy of Vanadium Tetracyanoethylene. *Microsc. Microanal.* **2020**, *26*, 3112−3114.

(64) Poole, C. P. *Electron Spin Resonance: A Comprehensive Treatise on Experimental Techniques*; Interscience Publishers: New York, 1967.

(65) *Quantitative EPR*; Eaton, G. R.; Eaton, S. S.; Barr, D. P.; Weber, R. T., Eds.; Springer: Wien, New York, 2010.